applied optics

Infrared atmospheric sounder interferometer radiometric noise assessment from spectral residuals

Carmine Serio,[1,2,*] Carsten Standfuss,[3] Guido Masiello,[1,2] Giuliano Liuzzi,[1] Emmanuel Dufour,[3] Bernard Tournier,[3] Rolf Stuhlmann,[4] Stephen Tjemkes,[4] and Paolo Antonelli[5]

[1]Scuola di Ingegneria, Universitá della Basilicata, Potenza 85100, Italy
[2]CNISM, Unitá di Ricerca Universitá della Basilicata, Potenza 85100, Italy
[3]Noveltis, Labege 31670, France
[4]EUMETSAT, Darmstadt 64295, Germany
[5]SSEC, University of Wisconsin, Madison, Wisconsin 53706, USA
*Corresponding author: carmine.serio@unibas.it

The problem of characterizing and estimating the radiometric noise of satellite high spectral resolution infrared spectrometers from Earth views is addressed in this paper. A methodology has been devised which is based on the common concept of spectral residuals (Observations-Calculations) obtained after spectral radiance inversion for atmospheric and surface parameters. An in-depth analytical assessment of the statistical covariance matrix of the spectral residuals has been performed which is based on the optimal estimation theory. It has been mathematically demonstrated that the use of spectral residuals to assess instrument noise leads to an effective estimator, which is largely independent of possible departures of the observational covariance matrix from the true covariances. Application to the Infrared Atmospheric Sounder Interferometer has been considered. It is shown that Earth-view-derived observation errors agree with blackbody in-flight calibration. The spectral residuals approach also proved to be effective in characterizing noise features due to mechanical microvibrations of the beam splitter of the IASI instrument. © 2015 Optical Society of America

OCIS codes: (010.0280) Remote sensing and sensors; (010.5620) Radiative transfer; (280.4991) Passive remote sensing.

http://dx.doi.org/10.1364/AO.54.005924

1. INTRODUCTION

In the context of Earth-atmosphere sounding from satellite observations, the usual concept of spectral residuals (Observations-Calculations, or simply O-C) has been commonly used for checking the quality of atmospheric–surface retrievals. However, spectral residuals are correlated with observations themselves and may depend on the assumed inverse scheme to estimate atmospheric and surface parameters. It is also known that spectral residuals yield a biased representation of instrument noise (e.g., [1]), although the magnitude of this bias has not yet been assessed in depth. Furthermore, in the current practice of satellite remote sensing with high spectral resolution infrared observations, *ad hoc* assumptions, such as the use of *inflation* [2–4], may lead to representing instrument noise through scaled forms of the observational covariance matrix or even with the introduction of additive components to account for the forward model errors. Moreover, in some cases, the observational covariance matrix may not be correctly prescribed and *ad hoc* approximations are used, such as a diagonal

matrix rather than the full matrix including its off-diagonal elements. Thus, the question is posed on how spectral residuals are dependent on the details of the given inverse scheme and whether they can be used to estimate instrument noise.

A feasibility analysis of the spectral residuals as a means to estimate the radiometric noise was performed in [2] in the context of the Infrared Atmospheric Sounder Interferometer (IASI [5]). Along the lines developed in [2], the present paper provides an in-depth analysis of the statistical properties of the spectral residuals arising from retrieval schemes where the matrix used to weight radiances is not necessarily equal to the true observational covariance matrix. The analysis is mostly intended to gain insight into understanding under which circumstances spectral residuals can be used to yield instrument noise. The methodology will be applied to IASI. The radiometric noise for IASI will be derived and compared with that obtained from in-flight blackbody calibration.

In particular, the methodology has been applied to IASI on Metop-A (Meteorological operational satellite A) to analyze the

error introduced by interferometer microvibrations and to assess the effect of the Centre National d'Etudes Spatiales (CNES) IASI instrument mode change on 25–26 November 2014 [6] to suppress this source of noise and related-induced distortion (the ghost effect, e.g., [7]) on the IASI instrumental spectral response function (ISRF).

It should be stressed that this paper mostly focuses on how to estimate the instrument or radiometric noise and should not be confused with the many *observation-error* analyses as normally conceived in the context of numerical weather prediction (NWP) operational assimilation systems (e.g., [3,4,8,9]), which deal with the sum of all errors relevant to the interpretation of the radiances in data assimilation. As a result, unlike our methodology, operational NWP observation-error methods largely overestimate the random component of the actual instrument noise of IASI [4]. However, it is fair to say that IASI ghost effects were first identified by NWP analyses of spatial patterns of IASI radiances which showed unexpected correlation [3]. A review of observation-error methods is beyond the scope of this paper, and the interested reader is referred to, e.g., [10].

This study deals with the derivation of a suitable estimator for the radiometric noise capable of covering the full spectral range of the instrument and not only a few sparse channels assimilated in NWP. The full spectral coverage is in fact needed to address aspects such as instrument engineering design and radiometric characterization, spectroscopy and forward modeling validation and tuning. Furthermore, we are mostly interested in designing and implementing an estimator sensitive to fine details of instrument noise. As an example, for IASI we are particularly interested in studying the noise at the merging of the IASI bands and in spectral regions where the atmosphere-emitted infrared spectrum may have sharp gradients because of strong molecular absorption (e.g., H_2O and CO_2 band heads at 6.7 and 4.3 μm, respectively).

Toward this objective, we have devised a rigorous mathematical approach. Based on this approach and its validation with experimental results, we demonstrate how the instrument noise of a satellite Fourier transform instrument can be derived from Earth views without strong additional hypotheses. We will show that the application of this approach to IASI yields an accurate and improved estimate of the radiometric noise, which compares to that derived from in-flight blackbody calibration. This new and improved characterization of the IASI noise is of great interest to a wide community. In fact, IASI is used as a standard or relative reference in many intercalibration studies to independently assess the radiance measurements of broad or narrowband instruments that share the same spectral region (e.g., [11–13]). Moreover, IASI noise characterization is also important in setting up new strategies to improve accuracy in global satellite observations (e.g., [14]). Finally, the assessment of IASI radiometric accuracy is of interest to analyses aiming at validating spectroscopy and tuning state-of-art forward models (e.g., [15,16]).

This work has been also motivated because the European Centre for the Exploitation of Meteorological Satellite (EUMETSAT) is preparing for the Meteorological Satellite (METEOSAT) Third Generation (MTG), which will carry the infrared sounder (IRS) at a hyperspectral sampling of 0.625 cm^{-1} wave numbers. The MTG-IRS instrument will be based on a Fourier transform spectrometer and two detector arrays, with one covering the long-wave and the other the mid-wave infrared bands. Each array consists of approximately 160×160 superdetectors after onboard aggregation of 3×3 elementary detectors. Radiometric accuracy and radiometric noise covariances might considerably vary over the 25,600 superdetectors, either due to detector responsivity variations across the array, or due to uncorrected instrument effects and/or residual processing errors, which will depend on the position of the superdetector within the array. For this reason, a simple but accurate methodology capable of at least identifying the problem from Earth-view only would be highly desirable.

Our analysis is based on the optimal estimation methodology described in [17], which we call δ-IASI. The methodology can deal with any number of IASI channels and the full, non-diagonal, observational covariance matrix prescribed for IASI. The δ-IASI methodology has been largely used and validated over the past few years [2,16,18–24].

The paper is organized as follows. Section 2 will briefly review the data used in the analysis and the salient features of the IASI instrument and its radiometric noise. The δ-IASI methodology is briefly reviewed in Section 3 for the aspects which are relevant to the mathematical derivation of the spectral residuals covariance matrix. Applications to IASI are shown in Section 4. Conclusions will be drawn in Section 5.

2. INSTRUMENT AND DATA

IASI [5] has been developed in France by CNES and is flying onboard the Metop platforms. These are satellites of the EUMETSAT European Polar System (EPS). IASI has been primarily put in orbit to work as a meteorological mission. Hence, its main objective is to provide suitable information on temperature and water vapor profiles. The instrument has a spectral coverage extending from 645 to 2760 cm^{-1}, which with a sampling interval $\Delta\sigma = 0.25$ cm^{-1} gives 8461 data points or channels for each single spectrum. IASI is a cross-track scanner, with thirty effective field of regard (FOR) per scan, which spans an angle range of $\pm 48.33°$ on either side of nadir; the two symmetric nadir FORs at angles of $\pm 1.67°$. Each FOR consists of a 2×2 matrix of so-called instantaneous fields of view (IFOV). Each IFOV has a diameter of 14.65 mrad, which corresponds to a ground resolution of 12 km at nadir and a satellite altitude of 819 km. The 2×2 matrix is centered on the viewing direction. At nadir, the FOR of four IASI pixels project at the ground a square area of ≈ 50 km $\times$ 50 km. More details on IASI and its mission objectives can be found in [5].

The data we use in this analysis have been acquired by the IASI instrument on Metop-A. The radiometric noise of IASI is regularly updated and checked through in-flight blackbody calibration. This is level 1C noise which applies to IASI apodized radiances. Figure 1 shows the IASI radiometric noise update of November 2012 [7] both in units of noise equivalent difference radiance (NEDR) and noise equivalent difference temperature (NEDT) at a scene temperature of 280 K.

Because of Gaussian apodization [25], IASI level 1C radiances are correlated. The correlation introduced by apodization is shift-invariant. That is, it does not depend on the wave
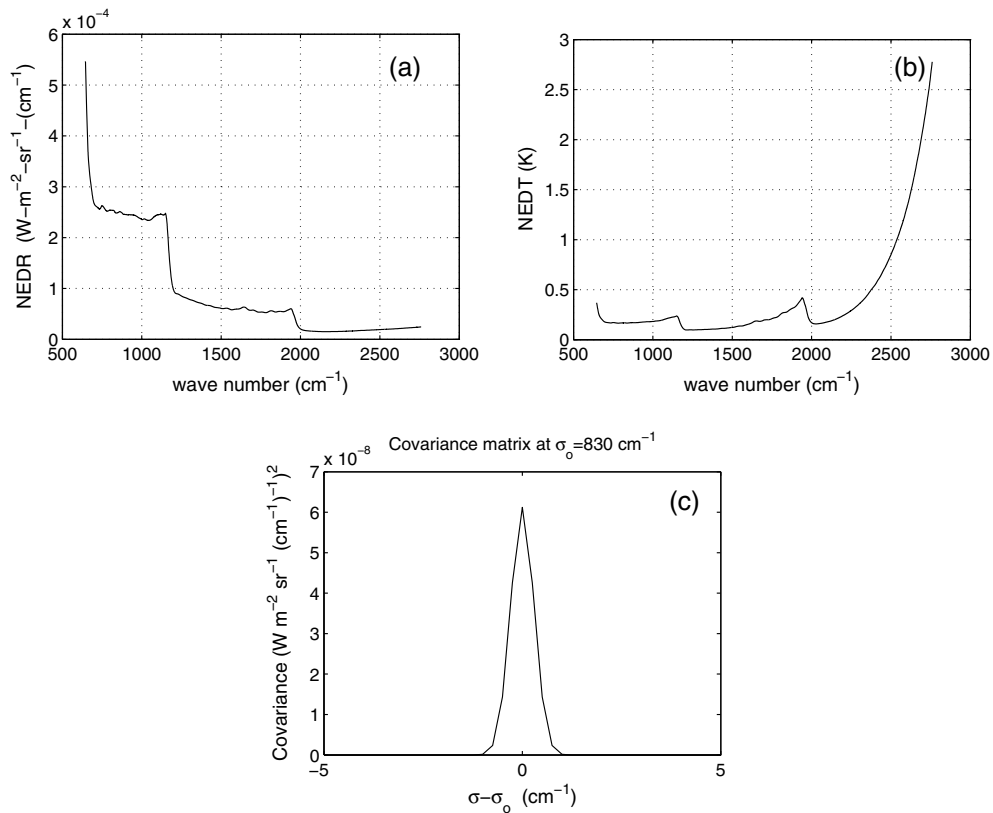
Fig. 1. (a) IASI radiometric noise for level 1C of apodized radiances in NEDR units. (b) As in (a) but in NEDT units at a scene temperature of 280 K. (c) Covariance of IASI at $\sigma_o = 830$ cm^{-1} for level 1C of apodized radiances.

number. To exemplify the length scale and shape of the correlation, Fig. 1(c) shows the covariance corresponding to $\sigma_o = 830$ cm^{-1} and neighboring wave numbers.

In this analysis, we will consider the full nondiagonal IASI covariance matrix. The square root of the diagonal of this matrix will be referred to as the IASI level 1C radiometric noise or simply *the radiometric noise*. To refer to both diagonal and nondiagonal terms, we will use the standard term of observational covariance matrix.

The IASI level 1C noise shown in Fig. 1 is that provided to end-users by CNES and it is meant to be the best characterization of the instrument radiometric noise available after the engineering assessment of IASI hardware and software. In this respect, the CNES release for IASI level 1C noise has to be considered as an upper limit to the IASI effective random noise, which in effect is smaller than what is normally checked with in-flight blackbody calibration.

The conservative upper limit radiometric noise shown in Fig. 1 is obtained through an *ad hoc* additive pseudo-noise component, the magnitude of which is based on preflight allocations for the impact of residual spectral calibration errors, microvibrations, and other instrument instabilities affecting the instrument spectral response. This theoretical specification-based pseudo noise (inaccessible from blackbody radiance monitoring) is added to the radiometric noise (the diagonal of the covariance matrix). However, its correlation effect is not modeled in the CNES release of the IASI covariance matrix [see e.g., Fig. 1(c)], which in fact considers the effect of

apodization alone (affecting four spectral samples on each side of the current one).

Microvibrations yield correlated errors and perturb (the ghost effect) the ISRF. The amplitude of these microvibrations was characterized by CNES on ground and is routinely monitored in-flight through analysis of the imaginary spectrum residual. The ghost origin is understood to be due to microvibrations of the beam splitter. The ghost affects the ISRF basically by replicating it at about ± 14 cm^{-1}. Normally, the amplitude of these replications is very low with respect to the ISRF maximum value. The amplitude and the central wave number of ISRF replications are functions of cube corner velocity, frequency, and mechanical amplitude of the beam splitter vibration (with an additional dependence on the current wave number or spectral sample).

Although compliant with user requirements [6], the ghost effect has been revealed by accurate analysis of IASI observations (e.g., [3]). Also, because of user evidence, CNES [6] has reanalyzed the IASI hardware functional system in order to take actions which could lead to suppress microvibrations. The CNES analysis concluded that microvibrations are dominated by the compensation device (CD) mechanical stress generated by the IASI cube corner mechanism. Consequently, the CD mechanism was switched off for two days (25–26 November 2014). The analysis of in-flight blackbody spectra recorded during the CD OFF event showed that the microvibration-induced error was largely suppressed. A report on the CNES analysis can be found in [6].

Also with the aim of analyzing the impact of the CD mode change (from ON to OFF) on the IASI radiometric noise, we have selected IASI observations on 22 July 2007 (CD ON) and 25 November 2014 (CD OFF).

The observations on 22 July 2007 are nadir, clear sky, sea surface spectra recorded over the Pacific Ocean (see Fig. 2 for details). We have a total of 44 spectra which stretches over a latitude/longitude box of 8.0° × 2.0°. These spectra are used for reference to qualify the IASI radiometric noise with CD ON.

The observations on 25 November 2014 consist of 11 clear sky consecutive scan lines, with spectra belonging to FORs within the view angle range of ±11.67°. The footprints are shown in Fig. 2. They cover a latitude/longitude box of 5.5° × 5.0° for a total of 352 IASI spectra.

Finally, we have also acquired in-flight blackbody IASI spectra corresponding to CD ON (three consecutive monthly external calibration periods—six complete orbits—from November 2013 to January 2014 for a total of 31,183 spectra per detector), and at the time of the CD OFF event (25–26 November 2014, for a total of 10,400 spectra per detector).

3. METHODOLOGICAL BACKGROUND

To begin with, we briefly summarize the basic aspects of the forward model. Then, we describe the basic equations of the retrieval methodology. Finally, we present the analytical derivation of the covariance of the spectral residual.

A. Forward Model

The forward model we use in the analysis is called σ-IASI [19]. This is a monochromatic forward module using a look-up table for the optical depth. The look-up table is derived from the line-by-line radiative transfer model (LBLRTM) [26]. For the shown work here, we used LBLRTM version 12.2. The forward module is based on 60 pressure layers, spanning the atmosphere from the ground level to the top assumed to be at 0.005 hPa. The model computes spectral radiances and analytical Jacobian derivatives of any surface and/or atmospheric parameter. IASI radiances are obtained through convolution with the IASI ISRF [5,25]. The accuracy and performance

Fig. 2.   Footprints of the IASI spectra used in the present work.

of the model applied to IASI has been discussed in [16,21], which the interested reader is referred to for further details.

B. Retrieval Methodology: Basic Equations and Definitions

The optimal estimator that we use to get an estimate of the state vector $\mathbf{v}$ from spectral radiances was first derived in [17] and discussed at a length in [2,21]. It reads,

$$(\gamma \mathbf{S}_a^{-1} + \mathbf{K}^t \mathbf{S}_\varepsilon^{-1} \mathbf{K})\mathbf{x} = \mathbf{K}^t \mathbf{S}_\varepsilon^{-1} \mathbf{y}, \tag{1}$$

where the superscript t indicates the transpose operation. Without any loss of generality, we assume that we are in a region around the first guess in which Eq. (1) is linear. If not, the scheme has to be further iterated according to the usual Gauss–Newton scheme (e.g., [17]). With this in mind, in Eq. (1) we have

$$\mathbf{x} = \hat{\mathbf{v}} - \mathbf{v}_a; \qquad \mathbf{y} = (\mathbf{R} - \mathbf{r}_0) - \mathbf{K}\mathbf{x}_a; \qquad \text{with } \mathbf{x}_a = \mathbf{v}_a - \mathbf{v}_0, \tag{2}$$

where $\hat{\mathbf{v}}$, $\mathbf{v}_a$, $\mathbf{v}_0$ are the state vector (estimated), the *a priori* or background vector, and the first guess state vector, respectively (the size of these vectors will be denoted with N). Furthermore, $\mathbf{S}_\varepsilon$ in Eq. (1) is the observational covariance matrix and $\mathbf{S}_a$ indicate a suitable smoothing operator, normally fixed to the covariance matrix of $\mathbf{v}_a$ (e.g., [1]). $\mathbf{R}$ is the vector (size M) of observed radiances, $\mathbf{r}_0 = F(\mathbf{v}_0)$, with F as the forward model. For the observations, we assume a signal–noise additive model:

$$\mathbf{R} = \mathbf{r} + \boldsymbol{\varepsilon}, \tag{3}$$

where $\mathbf{r}$ is the signal and $\boldsymbol{\varepsilon}$ a Gaussian noise term with zero mean and known covariance, $\mathbf{S}_\varepsilon$,

$$E(\boldsymbol{\varepsilon}) = 0; \qquad E(\boldsymbol{\varepsilon}\boldsymbol{\varepsilon}^t) = \mathbf{S}_\varepsilon, \tag{4}$$

where $E(\cdot)$ denotes statistical expectation. We also consider that the forward model can be biased:

$$F(\mathbf{v}) + \mathbf{b}_f = \mathbf{r}, \tag{5}$$

where $\mathbf{b}_f$ is a spectrally dependent bias term, assumed to be independent of the noise term $\boldsymbol{\varepsilon}$. Finally, the $M \times N$ derivative matrix or Jacobian $\mathbf{K}$ is computed as

$$\mathbf{K} = \frac{\partial F(\mathbf{v})}{\partial \mathbf{v}}\bigg|_{\mathbf{v}=\mathbf{v}_0}.$$

In dealing with the statistical properties of Eq. (1), we also need to specify a model for the background vector. In the context of NWP data assimilation, the background vector is assumed to obey an additive signal–noise model (e.g., [9]):

$$\mathbf{v}_a = \mathbf{v} + \boldsymbol{\varepsilon}_a, \tag{6}$$

where $\mathbf{v}$ is the true state. In this context, $\mathbf{v}_a$ is the forecast produced by a NWP dynamical model and $\mathbf{S}_a$ is the forecast error. Consistent with the model Eq. (6), we have $E(\mathbf{v}_a) = \mathbf{v}$ and the background noise can be defined as usual as the deviation of the given realization from its mean value:

$$\boldsymbol{\varepsilon}_a = \mathbf{v}_a - E(\mathbf{v}_a). \tag{7}$$

However, in the case where the background is specified through climatology, $\mathbf{v}_a$ is just the average of an ensemble of states and $\mathbf{S}_a$ yields its *meteorological* variability. In this case, it would be better to use
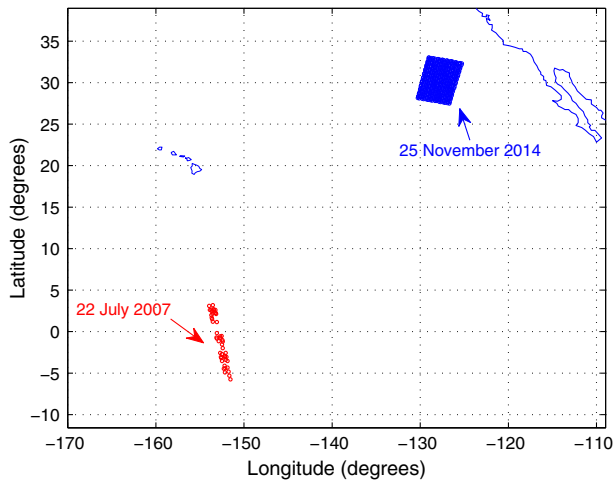
$$\mathbf{v} = \mathbf{v}_a + \boldsymbol{\varepsilon}_a, \tag{8}$$

since the weather variability is inherent to $\mathbf{v}$ rather than $\mathbf{v}_a$. If we compare Eq. (6) with Eq. (8) we see that they can be reconciled by substituting $\boldsymbol{\varepsilon}_a$ for $-\boldsymbol{\varepsilon}_a$. In the case where the noise probability density function is symmetric (as we do assume), this would imply no change in the statistical properties of the retrieval estimator whether we use Eq. (6) or Eq (8).

If we define

$$\tilde{\mathbf{S}}_\varepsilon = \gamma \mathbf{S}_\varepsilon, \tag{9}$$

then (e.g., [2]), Eq. (1) can be written in the equivalent form

$$(\mathbf{S}_a^{-1} + \mathbf{K}^t \tilde{\mathbf{S}}_\varepsilon^{-1} \mathbf{K})\mathbf{x} = \mathbf{K}^t \tilde{\mathbf{S}}_\varepsilon^{-1} \mathbf{y}, \tag{10}$$

which suggests that scaling the background covariance by $1/\gamma$ has the same effect as scaling the observational covariance matrix by γ.

The explicit introduction of $\tilde{\mathbf{S}}_\varepsilon$ in place of $\mathbf{S}_\varepsilon$ also affects the statistical properties (mean, covariance, and averaging kernels) of the retrieval estimator. These have been discussed and derived at a length in [2,17]. They are summarized here for completeness and benefit of the reader.

Defining

$$\mathbf{A} = (\mathbf{S}_a^{-1} + \mathbf{K}^t \tilde{\mathbf{S}}_\varepsilon^{-1} \mathbf{K}), \quad \mathbf{B} = \mathbf{K}^t \tilde{\mathbf{S}}_\varepsilon^{-1}, \tag{11}$$

we easily derive

$$E(\hat{\mathbf{v}}) = E(\mathbf{v}_a) + \mathbf{A}^{-1}\mathbf{B}\mathbf{b}_f. \tag{12}$$

In the case where Eq. (6) applies and the forward model is unbiased, we have $E(\hat{\mathbf{v}}) = \mathbf{v}$, and the retrieval is unbiased.

For the covariance $\mathbf{S}_{\hat{v}}$ of $\hat{\mathbf{v}}$, we have [2,17]

$$\mathbf{S}_{\hat{v}} = \mathbf{A}^{-1}(\mathbf{B}\mathbf{S}_\varepsilon \mathbf{B}^t + \mathbf{S}_a^{-1})\mathbf{A}^{-1}. \tag{13}$$

Once again we stress that we distinguish between $\tilde{\mathbf{S}}_\varepsilon$ and $\mathbf{S}_\varepsilon$, with the latter being the true observational covariance matrix. In addition, we stress that the validity of Eq. (13) is not limited to the scaling case of Eq. (9) but applies to any conceivable $\tilde{\mathbf{S}}_\varepsilon$. In the case where $\tilde{\mathbf{S}}_\varepsilon = \mathbf{S}_\varepsilon$, we recover the usual result for the *a posteriori* retrieval covariance matrix $\mathbf{S}_{\hat{v}} = \mathbf{A}^{-1}$ [1].

For the averaging kernels, we have [2,17]

$$\frac{\partial \hat{\mathbf{v}}}{\partial \mathbf{v}} = \mathbf{A}^{-1}\mathbf{B}\mathbf{K}. \tag{14}$$

C. Spectral Residuals Covariance

Considering expectation values of $\hat{\mathbf{v}}$ given by Eq. (1), it is important to realize that the retrieval estimator is subject to two sources of random noise: the observational noise $\boldsymbol{\varepsilon}$ and the background noise $\boldsymbol{\varepsilon}_a$. These two sources of noise (assumed uncorrelated) govern the random fluctuations of $\hat{\mathbf{v}}$. Therefore, the computation of expectation values has to consider the joint variation of both terms.

Keeping this in mind, the spectral residuals for a given retrieved state $\hat{\mathbf{v}}$ is defined according to

$$\delta \mathbf{y} = \mathbf{R} - F(\hat{\mathbf{v}}). \tag{15}$$

Assuming that the estimated state vector $\hat{\mathbf{v}}$ is in the linear retrieval region around the true state vector $\mathbf{v}$, we have

$$F(\mathbf{v}) = F(\hat{\mathbf{v}}) + \mathbf{K}(\mathbf{v} - \hat{\mathbf{v}}) + \text{higher order terms}, \tag{16}$$

where now

$$\mathbf{K} = \left. \frac{\partial F(\mathbf{v})}{\partial \mathbf{v}} \right|_{\mathbf{v}=\hat{\mathbf{v}}}.$$

Using Eq. (16), we can write the spectral residual according to

$$\delta \mathbf{y} = (\mathbf{R} - F(\mathbf{v})) + \mathbf{K}(\hat{\mathbf{v}} - \mathbf{v})$$
$$= (\mathbf{R} - F(\mathbf{v})) + \mathbf{K}(\mathbf{v} - \mathbf{v}_a) - \mathbf{K}(\hat{\mathbf{v}} - \mathbf{v}_a), \tag{17}$$

which, apart from the forward model bias is not affecting the analytical derivation of the covariance, can be written as

$$\delta \mathbf{y} = \boldsymbol{\varepsilon} - \mathbf{K}\boldsymbol{\varepsilon}_a - \mathbf{K}(\hat{\mathbf{v}} - \mathbf{v}_a). \tag{18}$$

The term $(\hat{\mathbf{v}} - \mathbf{v}_a)$ can be easily related to observational and background noise by Eq. (1). In fact, considering Eq. (3) and linearizing the forward model, we obtain from Eq. (1)

$$\mathbf{A}(\hat{\mathbf{v}} - \mathbf{v}_a) = \mathbf{B}(\boldsymbol{\varepsilon} - \mathbf{K}\boldsymbol{\varepsilon}_a), \tag{19}$$

with $\mathbf{A}$ and $\mathbf{B}$ defined in Eq. (11). Substituting Eq. (19) into Eq. (18) and rearranging terms we have

$$\delta \mathbf{y} = (\mathbf{I} - \mathbf{K}\mathbf{A}^{-1}\mathbf{B})(\boldsymbol{\varepsilon} - \mathbf{K}\boldsymbol{\varepsilon}_a). \tag{20}$$

The covariance of the spectral residuals easily follows considering the expectation $E(\delta \mathbf{y} \delta \mathbf{y}^t)$,

$$E(\delta \mathbf{y} \delta \mathbf{y}^t) = \mathbf{S}_{\delta y} = (\mathbf{I} - \mathbf{K}\mathbf{A}^{-1}\mathbf{B})(\mathbf{S}_\varepsilon + \mathbf{K}\mathbf{S}_a\mathbf{K}^t)(\mathbf{I} - \mathbf{K}\mathbf{A}^{-1}\mathbf{B})^t, \tag{21}$$

which can be further simplified (see Appendix A) to give

$$\mathbf{S}_{\delta y} = \mathbf{S}_\varepsilon - \mathbf{K}\mathbf{A}^{-1}\mathbf{K}^t - (\mathbf{S}_\varepsilon - \tilde{\mathbf{S}}_\varepsilon)\tilde{\mathbf{S}}_\varepsilon^{-1}\mathbf{K}\mathbf{A}^{-1}\mathbf{K}^t - \mathbf{K}\mathbf{A}^{-1}\mathbf{K}^t\tilde{\mathbf{S}}_\varepsilon^{-1}(\mathbf{S}_\varepsilon - \tilde{\mathbf{S}}_\varepsilon)$$
$$+ \mathbf{K}\mathbf{A}^{-1}\mathbf{K}^t\tilde{\mathbf{S}}_\varepsilon^{-1}(\mathbf{S}_\varepsilon - \tilde{\mathbf{S}}_\varepsilon)\tilde{\mathbf{S}}_\varepsilon^{-1}\mathbf{K}\mathbf{A}^{-1}\mathbf{K}^t. \tag{22}$$

Once again, we note that we distinguish between $\tilde{\mathbf{S}}_\varepsilon$ [imposed on the retrieval scheme, e.g., Eq. (10)] and the actual observational noise covariance, $\mathbf{S}_\varepsilon$.

In the case where $\tilde{\mathbf{S}}_\varepsilon = \mathbf{S}_\varepsilon$, Eq. (22) becomes

$$\mathbf{S}_{\delta y} = \mathbf{S}_\varepsilon - \mathbf{K}\mathbf{S}_{\hat{v}}\mathbf{K}^t, \tag{23}$$

where, as before, $\mathbf{S}_{\hat{v}} = \mathbf{A}^{-1}$ is the *a posteriori* covariance of the retrieved state. The meaning of Eq. (23) is straightforward and quite natural. Because the retrieved state vector is correlated with observations, the statistical variability of O-C is not that of O alone. We have also to consider an additional, negative, term which is the projection into the data space of the retrieval covariance matrix.

In passing, we note that Eq. (23) can be also written (see Appendix A) according to

$$\mathbf{S}_{\delta y} = \mathbf{S}_\varepsilon - \mathbf{K}\mathbf{S}_{\hat{v}}\mathbf{K}^t = \mathbf{S}_\varepsilon(\mathbf{K}\mathbf{S}_a\mathbf{K}^t + \mathbf{S}_\varepsilon)^{-1}\mathbf{S}_\varepsilon. \tag{24}$$

This alternate formula is only quoted here for a proper comparison with previous work on the subject (e.g., see [1] on page 89, Eq. 5.27).

Equation (23) reveals that the spectral residuals estimator underestimates $\mathbf{S}_\varepsilon$. However, in general for an instrument such as IASI, the negative term in Eq. (24) is negligible in comparison with $\mathbf{S}_\varepsilon$. This can be appreciated from Fig. 3 which compares the square root of the diagonal elements (i.e., the usual radiometric noise) of $\mathbf{S}_{\delta v}$ given by Eq. (23) and $\mathbf{S}_\varepsilon$, respectively. The computation refers to a sea surface, clear sky and nadir view, tropical air mass whose state vector (temperature, water vapor, and ozone) is shown in Fig. 4. The corresponding skin
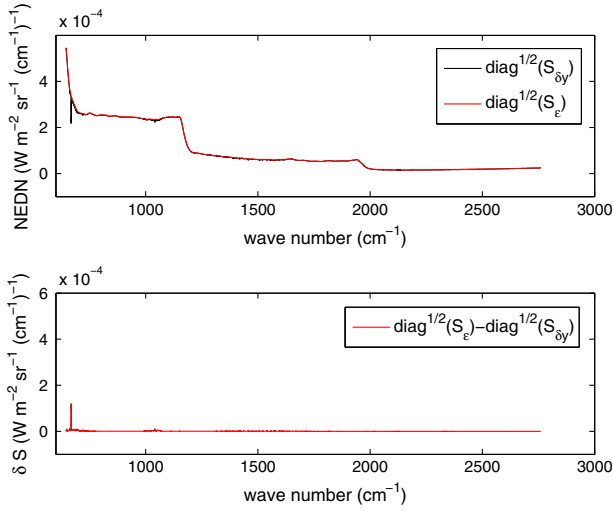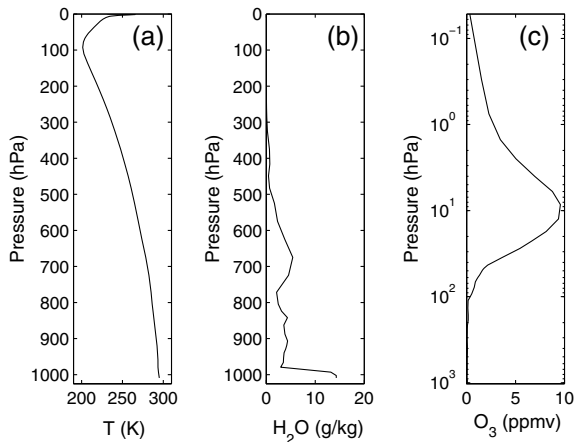
Fig. 3. Case where $\tilde{\mathbf{S}}_\varepsilon = \gamma \mathbf{S}_\varepsilon$, with $\gamma = 1$. Upper panel, comparison of the square root of the diagonal of the two matrices $\mathbf{S}_\varepsilon$ and $\mathbf{S}_{\delta y}$. Lower panel, difference between the square root of the two diagonals.

Fig. 5. Same as Fig. 2, but now the square root of the diagonal elements of $\mathbf{S}_{\delta y}$ has been smoothed with a moving average filter with a window width of 2.5 cm^{-1}.
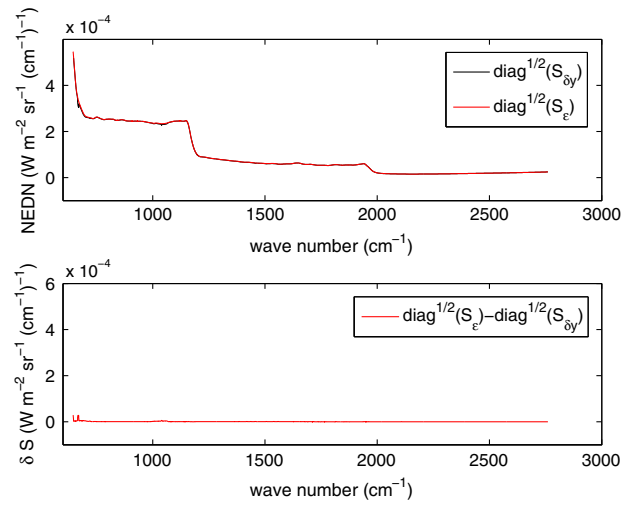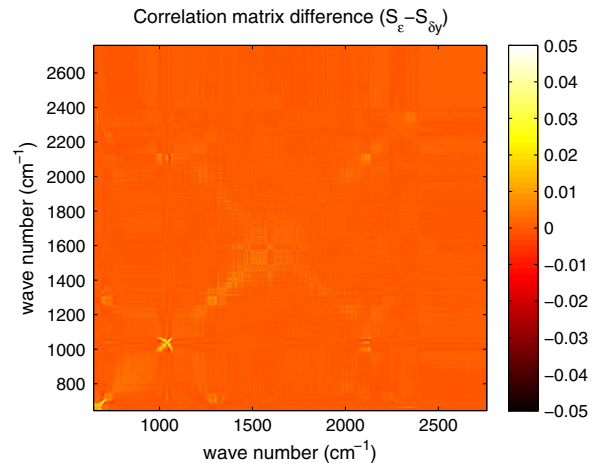
temperature is 297.11 K and the surface emissivity used in the radiative transfer is that of the Masuda model [27].

We see that the difference between the diagonals of the two matrices is negligible almost everywhere within the IASI spectral coverage, except around 667 cm^{-1}, which is the center of the most intense CO_2 Q-branch in the long-wave region. This can be explained because the 667 cm^{-1} CO_2 Q-branch is sensitive to the whole atmospheric stratosphere (e.g., [23]). Therefore, when the retrieval error, $\mathbf{S}_{\hat{x}}$, is mapped back to the radiance space, the region around 667 cm^{-1} receives positive and coherent contributions from the temperature error profile in a wide altitude range encompassing the whole stratosphere. Although less pronounced than that at 667 cm^{-1}, a relatively larger negative bias is also seen in the O_3 absorption band (around 1040 cm^{-1}), which again is explained by the sensitivity of this spectral region to a relatively large portion of the stratospheric temperature (hence, error) profile.

The difference between the diagonals of the two matrices has a spiky, spectrally resolved structure (barely seen in Fig. 3,

but visible when zooming locally), unlike the original IASI radiometric noise. As shown in Fig. 5, this spiky bias can be removed by applying a simple smoothing filter, such as a moving average filter (that is applied in Fig. 5 with a window width of 2.5 cm^{-1}). After the application of this filter, we see that the negative spike is largely suppressed everywhere across the IASI spectral coverage. The difference is also negligible over off-diagonal terms, as it is possible to see from Fig. 6 which shows the difference of the two correlation matrices corresponding to $\mathbf{S}_\varepsilon$ and $\mathbf{S}_{\delta y}$. An excess correlation is seen that does not exceed ±0.03.

In the case where $\tilde{\mathbf{S}}_\varepsilon = \gamma \mathbf{S}_\varepsilon$ (scaling case), Eq. (22) becomes

$$\mathbf{S}_{\delta y} = \mathbf{S}_\varepsilon + \frac{\gamma - 2}{\gamma} \mathbf{K} \mathbf{A}^{-1} \mathbf{K}^t + \frac{1 - \gamma}{\gamma} \mathbf{K} \mathbf{A}^{-1} \mathbf{K}^t \tilde{\mathbf{S}}_\varepsilon^{-1} \mathbf{K} \mathbf{A}^{-1} \mathbf{K}^t, \quad (25)$$

which compared to Eq. (23) shows that the use of an inflation or scaling parameter $\gamma > 1$ tends to compensate the effect of bias. In fact, for $\gamma > 2$ the second term in Eq. (25) is positive,


Fig. 4. Atmospheric state vector used for the analysis shown in Fig. 3. (a) Temperature, (b) water vapor, and (c) ozone.

Fig. 6. Case where $\tilde{\mathbf{S}}_\varepsilon = \gamma \mathbf{S}_\varepsilon$, with $\gamma = 1$. Color map of the difference between the correlation matrices corresponding to $\mathbf{S}_\varepsilon$ and $\mathbf{S}_{\delta y}$.

whereas the third ones is negative. This effect can be appreciated in Fig. 7 where, again for the state vector shown in Fig. 4, we compare the square root of the two diagonals of $\mathbf{S}_{\delta y}$ and $\tilde{\mathbf{S}}_\varepsilon$ for $\gamma = 0.1, 1, 2, 3, 10$. For $\gamma = 2$, we have that the second terms in Eq. (25) just vanishes. Figure 7 clearly shows that the

effect of bias is negligible over a range of γ spanning 2 orders of magnitude.

We have found that the bias is negligible also for nonscaling cases. A common nonscaling case is that in which $\tilde{\mathbf{S}}_\varepsilon$ is built up with the diagonal of $\mathbf{S}_\varepsilon$ alone. For IASI this corresponds to
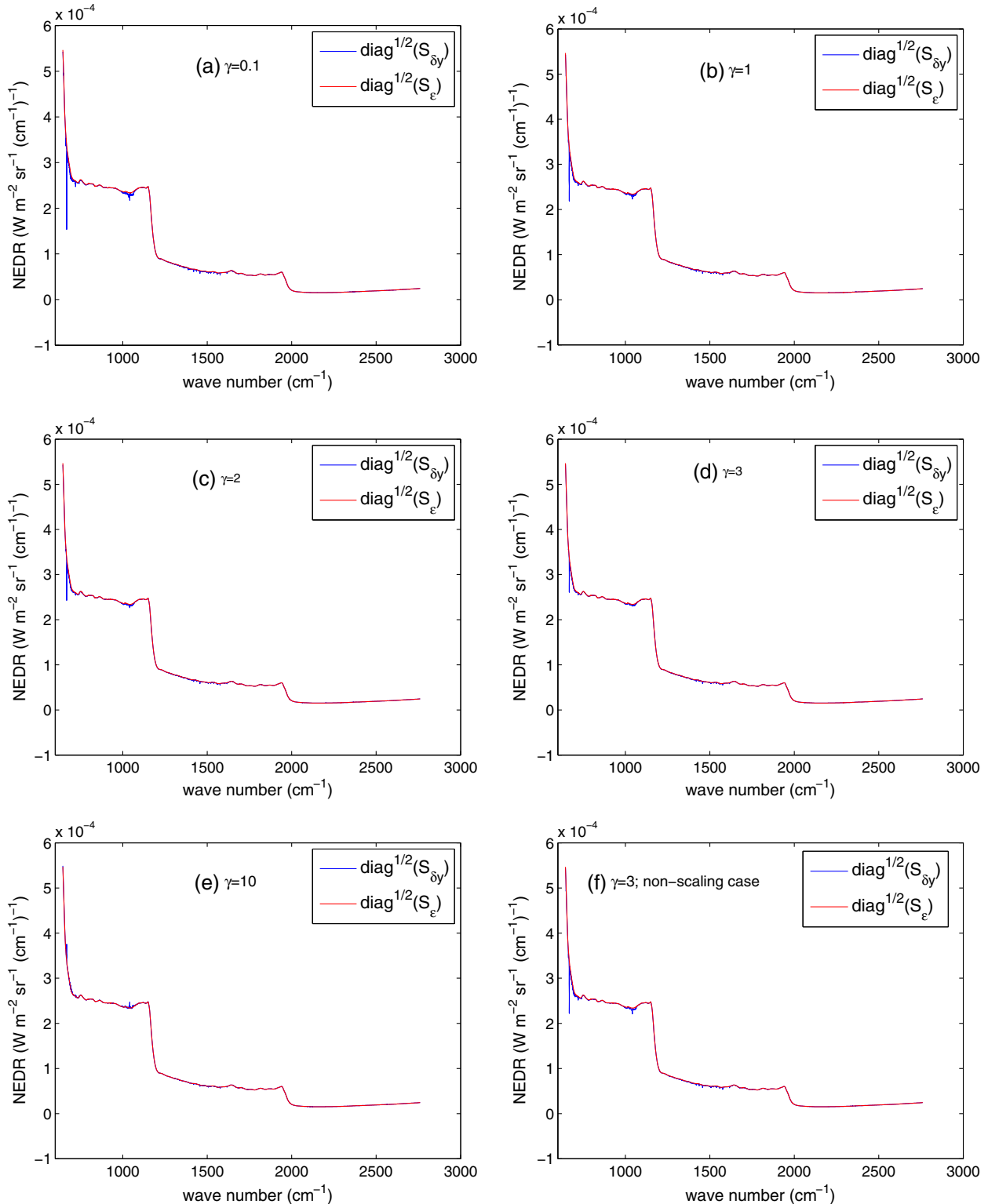
Fig. 7.   From (a)–(e), case where $\tilde{\mathbf{S}}_\varepsilon = \gamma \mathbf{S}_\varepsilon$; comparison of $\mathrm{diag}^{1/2}(\mathbf{S}_\varepsilon)$ with $\mathrm{diag}^{1/2}(\mathbf{S}_{\delta y})$ for $\gamma = 0.1$, $\gamma = 1$, $\gamma = 2$, $\gamma = 3$, and $\gamma = 10$. Panel (f) corresponds to the a nonscaling case with $\tilde{\mathbf{S}}_\varepsilon = \gamma\, \mathrm{diag}(\mathbf{S}_\varepsilon)$, where $\gamma = 3$.

ignoring off-diagonal terms, a simplification which is commonly used to avoid the heavy computational burden related to an observational matrix whose size can be as high as 8461 × 8461. The results of applying to this a nonscaling case are exemplified in Fig. 7(f). The analysis has been obtained through a direct application of the general formula of Eq. (21), and the case shown in Fig. 7(f) also includes an inflation parameter, $\gamma = 3$. In other words, the $\tilde{\mathbf{S}}_\varepsilon$ imposed on the retrieval is three times the diagonal of the true observational covariance matrix.

To sum up, we have that $\mathbf{S}_{\delta y}$ is fairly independent of any $\tilde{\mathbf{S}}_\varepsilon$ that we impose to the retrieval and we have $\mathbf{S}_{\delta y} \approx \mathbf{S}_\varepsilon$.

Before concluding this section, we also mention that the cross product between O-C and Observation-Background (O-B), namely, $(\mathbf{R} - F(\hat{\mathbf{v}}))(\mathbf{R} - F(\mathbf{v}_a))$ has been proposed by [9] in the context of NWP data assimilation as a diagnostic check of the departure of a given $\tilde{\mathbf{S}}_\varepsilon$ used in the retrieval scheme from the true $\mathbf{S}_\varepsilon$. Using the mathematical machinery that we have developed in this section, we can easily show that the expectation value of the cross product (O-C)(O-B) yields the true observational covariance matrix provided that $\tilde{\mathbf{S}}_\varepsilon = \mathbf{S}_\varepsilon$.

In the case where $\tilde{\mathbf{S}}_\varepsilon \neq \mathbf{S}_\varepsilon$, the expectation value may largely differ from $\mathbf{S}_\varepsilon$, as expected for a diagnostic tool. Furthermore, in general, the cross product (O-C)(O-B) is not symmetric and therefore cannot be used as an estimator of $\mathbf{S}_\varepsilon$ which is symmetric-definite.

D. Estimator for $\mathbf{S}_\varepsilon$

From Section 3.C we have seen that a statistical estimator for $\mathbf{S}_\varepsilon$ derived from the spectral residuals would be largely independent of the observational covariance matrix actually imposed on the retrievals.

A straightforward estimator can be built up by considering an ensemble of m retrieved states. If $\delta\mathbf{y}_i$, $i = 1, \ldots, m$ is the spectral residuals corresponding to the ith retrieval, we can define the spectral residuals matrix $\mathbf{X}$, whose columns are the vectors of the spectral residual, as

$$\mathbf{X} = (\delta\mathbf{y}_1, \ldots, \delta\mathbf{y}_i, \ldots, \delta\mathbf{y}_m). \qquad (26)$$

An estimate $\hat{\mathbf{S}}_{\delta y}$ of $\mathbf{S}_{\delta y}$ is given by

$$\hat{\mathbf{S}}_{\delta y} = \frac{1}{m}(\mathbf{X} - \bar{\mathbf{X}})(\mathbf{X} - \bar{\mathbf{X}})^t, \qquad (27)$$

where $\overline{\mathbf{X}}$ is the ensemble average of the spectral residual. Note that the ensemble is also important in estimating and removing the mean $\overline{\mathbf{X}}$, which includes the forward model bias as well.

In principle, in case the many sources of atmospheric and surface variability were properly represented in the retrieved state vector, estimator Eq. (27) would work for any time and space coverage of the ensemble used to define the spectral residuals matrix $\mathbf{X}$. However, there are two main limitations to the extension and size of the time–space coverage.

First, the forward model error is an additional source of potential random error, which can add extra variability to the (O-C)-derived observation error. The forward model is expected to be mostly dependent on the air mass type. Therefore, the above methodology should be applied to Earth-views with homogeneous air mass; tropical soundings should not be used together with polar air mass.

Second, not all the sources of atmospheric and surface variability are normally represented in the retrieved state vector. Generally, minor or trace gases are set to their climatology. Therefore, if we consider a time slot or a target area as large to allow for these nonrepresented constituents to change, then the spectral residuals would show that this variability summed to the radiometric noise. For the estimation of the observation error, it is not so important to have a good representation of nonretrieved parameters. It is much more important that they do not vary within the time slot considered for the spectral residuals analysis. Atmospheric–surface variability can be optimized but not completely zeroed. For optimization, we could consider clear sky, sea surface soundings in such a way as to minimize variability of the surface emissivity. Over sea surfaces, IASI Earth views, which are of short-time span, should be preferably selected.

In addition to space-localized Earth views, to further limit as much as possible unwanted additional sources of noise, we have adopted the following sampling strategy. The retrieval algorithm operates per IASI FOR, whose corresponding four spectra are obtained simultaneously over a sounding area of ≈ 50 km × 50 km in spatial extent. These four simultaneous spectra are inverted for geophysical parameters, the spectral residuals computed, and the matrix $\hat{\mathbf{S}}_{\delta y, \text{FOR}}$ for the single FOR is obtained according to Eq. (27). The analysis is repeated for m_{FOR} possibly space-contiguous FORs, and the final estimate is obtained according to

$$\hat{\mathbf{S}}_{\delta y} = \frac{1}{m_{\text{FOR}}} \sum_{\text{FOR}} \hat{\mathbf{S}}_{\delta y, \text{FOR}}. \qquad (28)$$

Finally, we stress again that the number of FOR boxes we consider are limited in space, as exemplified, e.g., in Fig. 2.

4. APPLICATION TO IASI

Figure 8 shows the radiometric noise estimate based on the 44 IASI spectra recorded on 22 July 2007, whereas Fig. 9 shows the results for the case study of 25 November 2014 (342 IASI spectra). The footprints of the IASI spectra belonging to both case studies are shown in Fig. 2.

We remark that the (simultaneous) retrieval of surface temperature (T_s) and atmospheric parameters [temperature (T), water vapor (Q), and ozone (O_3)] from these IASI spectra has been performed with the retrieval approach outlined in Section 3.B with the matrix $\mathbf{S}_a$ derived by climatology and with the observational covariance matrix $\tilde{\mathbf{S}}_\varepsilon$ set to the IASI level 1C covariance matrix as released by CNES (see, e.g., Fig. 1). An inflation parameter $\gamma = 3$ has been used. Emissivity is set to Masuda's model [27]. Furthermore, we have used ≈ 5000 IASI channels as shown in Fig. 10. We use the full IASI band 1 (645 to 1210 cm^{-1}), the R-branch of the H_2O absorption band at 6.7 μm (i.e., the spectral segment 1600 to 2000 cm^{-1}) which falls within IASI band 2. Of IASI band 3 (2000 to 2760 cm^{-1}), we only use the first segment, i.e., 2000 to 2260 cm^{-1}. The segment 1210 to 1600 cm^{-1} is not used because of CH_4 and N_2O absorption. These two species are not included in the retrieved state vector, which as mentioned includes T_s, T, Q, O_3. The rest of band 3, from 2260 cm^{-1} to the end of the IASI spectrum is not used because of non-LTE effects and solar
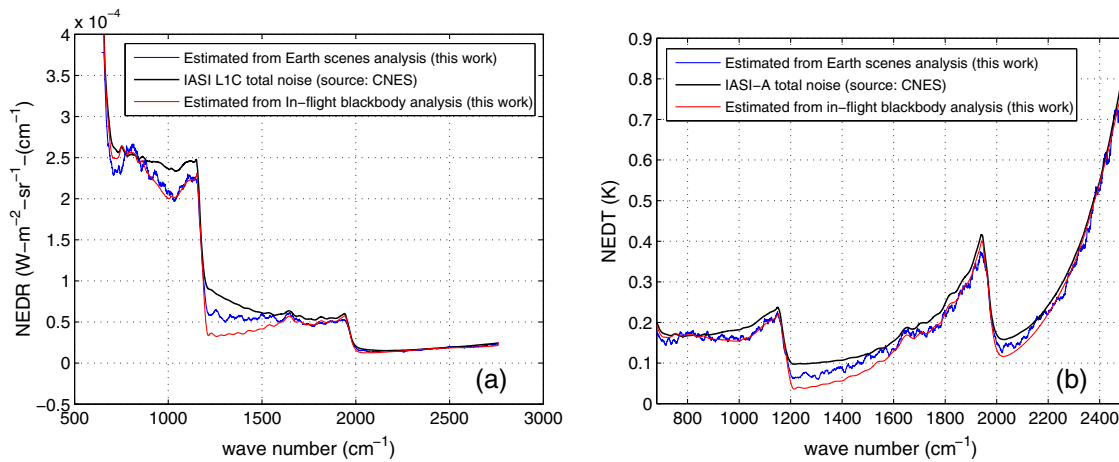
Fig. 8. Case study on 22 July 2007. Analysis of the IASI observation noise and comparison with the IASI radiometric noise as released by CNES. (a) The analysis is shown in units of NEDR. (b) The same analysis is shown in units of NEDT at a scene temperature of 280 K. The estimate from the Earth view analysis has been smoothed with a moving average filter with a window width of 2.5 cm^{-1}. The analysis refers to a time period when the interferometer CD was on.

contamination in the daytime. Finally, our channel selection corresponds closely to the MTG/IRS spectral coverage.

To begin with, we analyze the results corresponding to *the case study of 22 July 2007*. In Fig. 8, the estimated instrument noise is compared to the official CNES-IASI radiometric noise (imposed on the retrieval) and to the radiometric noise obtained by the direct analysis of in-flight blackbody spectra recorded from November 2013 to January 2014 (see Section 2).

We see that the O-C analysis correctly recovers magnitude and spectral patterns of the IASI noise in the three IASI bands. Both the analyses performed in this work (Earth view and blackbody) confirm that the IASI radiometric noise released by CNES overestimates the actual radiometric noise of the instrument.

Furthermore, the two analyses also show an anomalous noise excess around 800 cm^{-1}, which is not seen in the IASI noise released by CNES (see Fig. 8). This feature is consistent with the effect of ice deposition on the field lens at the entrance

of the IASI cold box. Although the two analyses are not for the same time, they both consider periods far from the decontamination procedure, which is regularly performed for IASI [7]. From Fig. 8, we also see a difference between Earth view and blackbody radiometric noise estimates in the spectral range of 1210–1600 cm^{-1}, which will be discussed below.

In passing, we note that the fact that our Earth-view case study refers to July 2007, whereas the in-flight blackbody spectra to November 2013–January 2014 gives also the opportunity to appreciate the stability of the IASI noise, hence high quality of the instrument.

The analysis corresponding to *the case study of 25 November 2014* (see Fig. 2) is shown in Fig. 9. Once again, we see an excellent agreement in the radiometric noise estimated from the spectral residuals with that directly computed from the in-flight blackbody spectra. This agreement is even more statistically significant due to (1) the enhanced number (342) of IASI atmospheric spectra used for our analysis and (2) the fact that the
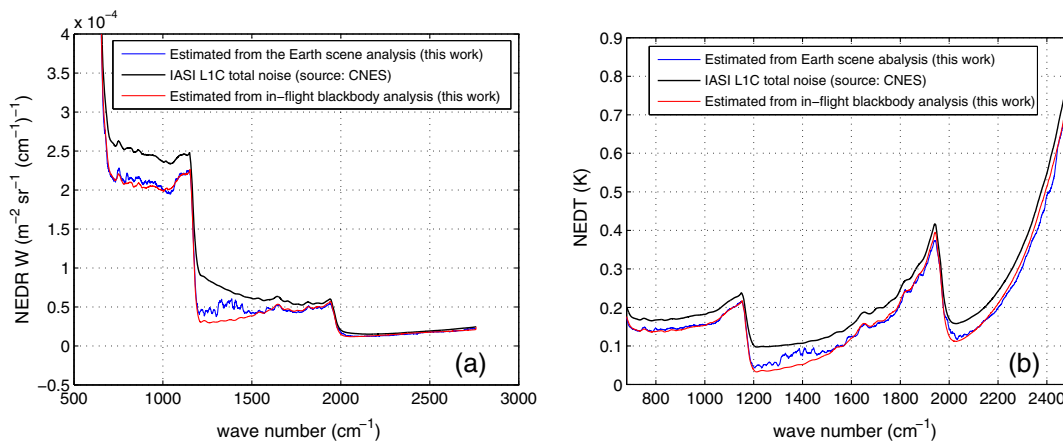

Fig. 9. Case study on 25 November 2014. Analysis of the IASI observation noise and comparison with the IASI radiometric noise as released by CNES. (a) The analysis is shown in units of NEDR. (b) The same analysis is shown in units of NEDT. The estimate from the Earth view analysis has been smoothed with a moving average filter with a window width of 2.5 cm^{-1}. The analysis refers to a time period when the interferometer CD was off.

blackbody spectra have been acquired in the same period (25–26 November 2014) as that for the Earth-view sounding. The two analyses show exactly the same features. Comparing the results in Fig. 9 to the analysis shown in Fig. 8, we see now that the ice contamination at 800 cm^{-1} is no longer visible. This is because decontamination occurred on the late days of September 2014. Furthermore, in agreement with the results shown in Fig 8, the analysis of Fig. 9 also confirms that the IASI radiometric noise released by CNES overestimates the real radiometric noise of the instrument.
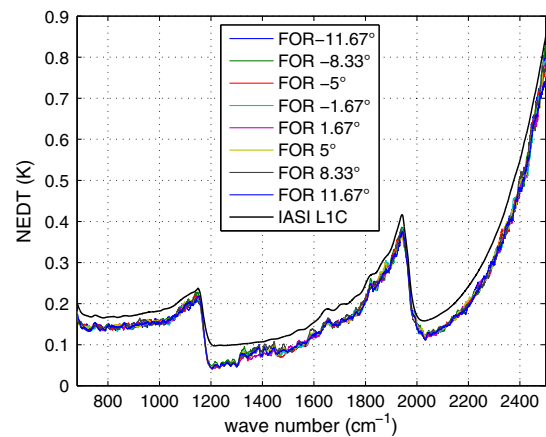
The IASI spectra recorded on 25 November 2014 allow us to check a possible dependence of the radiometric noise on the viewing angle. In fact, the spectra were obtained with the instrument scanning $\pm 11.67°$ on either side of nadir. Therefore, we have a total of eight diverse FORs. Considering that we have 11 consecutive scan lines, we get a total of 44 IASI spectra per FOR. The estimated IASI radiometric noise is shown in Fig. 11 from which we conclude that no evident dependence on the viewing angle is seen, at least within the angle range of $\pm 11.67°$.

The excellent agreement between Earth-view and in-flight blackbody analyses of the IASI noise shown in Figs. 8 and 9 made us confident in the use of the Earth-view-derived estimator for the analysis of the ghost effect because of microvibrations. These are expected to add significant structures in the spectral regions where instrument noise is low (i.e., higher signal-to-noise ratio). This occurs in particular at the long-wave side of IASI band 2 and, to a lesser extent, in band 3 (see Figs. 8 and 9). To analyze the presence of ghost structures, we computed the correlation matrix corresponding to $\hat{\mathbf{S}}_{\delta y}$ and subtracted from it the correlation matrix corresponding to $\tilde{\mathbf{S}}_{\varepsilon}$, imposed on the retrieval. In this case, we eliminate the correlation effect of apodization. The result is shown in Fig. 12 for the spectral range of 1150 to 1250 cm^{-1} corresponding to the merging region of IASI bands 1 and 2. In the case of no ghost, we would expect just random fluctuations with no evident structure.

Figure 12 provides a comparison among three cases: (a) CD ON (case study on 22 July 2007), (b) a ghost model simulation, and (c) CD OFF (case study on 25 November 2014). The simulation in Fig. 12(b) was obtained with a simple ghost
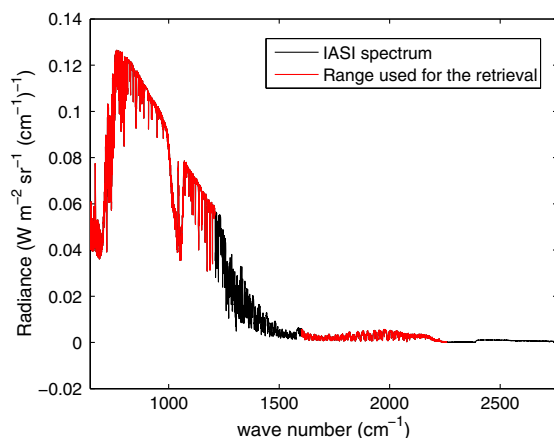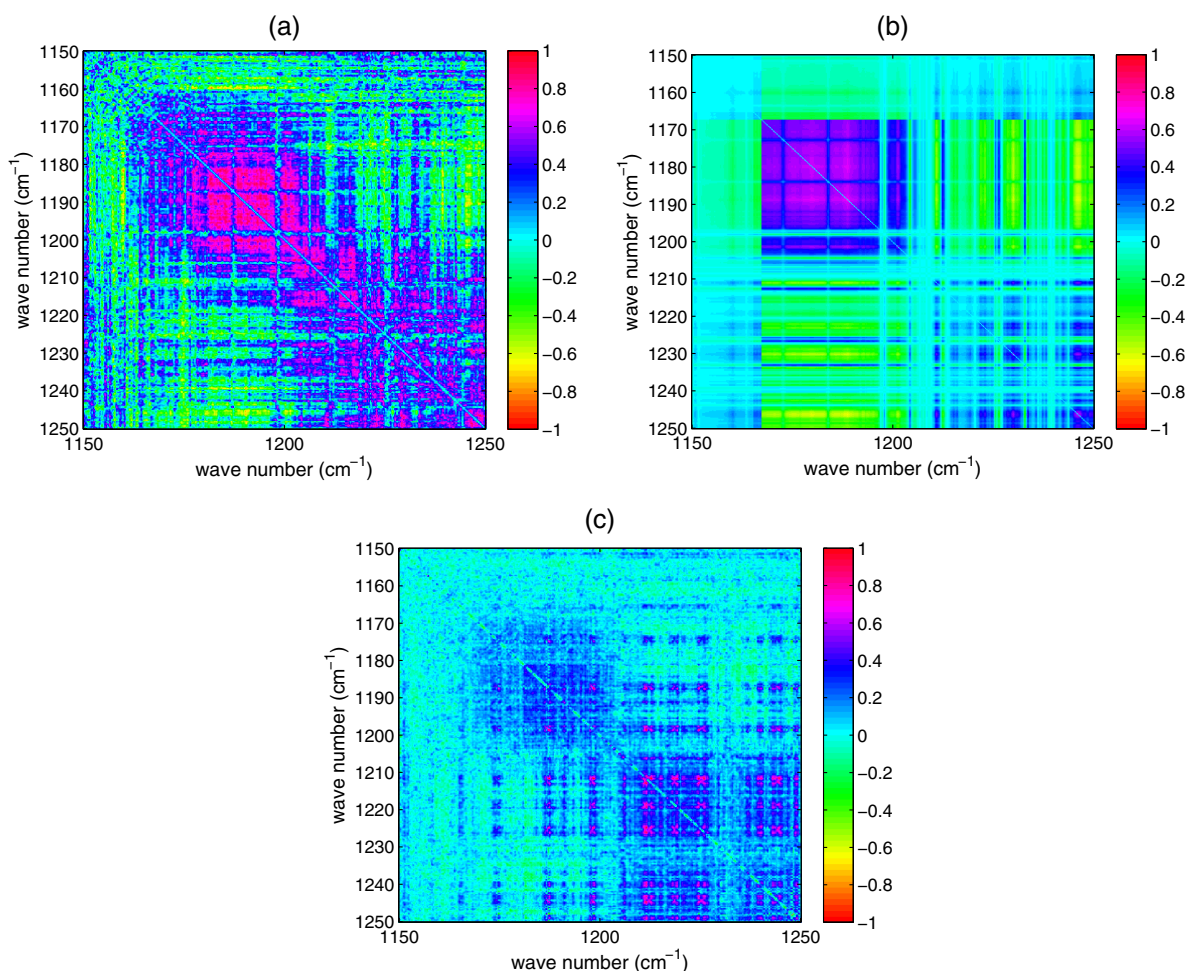

Fig. 11. IASI instrument noise (NEDT at a scene temperature of 280 K) as a function of the FOR derived from the analysis of the IASI spectra on 25 November 2014. The estimate has been smoothed with a moving average filter with a window width of 2.5 cm^{-1}. The figure also shows the comparison with the IASI level 1C noise (total noise) imposed on the retrieval analysis.

model compatible with IASI microvibrations, the optical transfer functions, and a representative atmospheric spectrum. A mathematical description of the ghost model is beyond the scope of this paper. The interested reader is referred to [28] for further details.

The comparison shows very good agreement in the CD ON case with the ghost model: the correlation structure is exactly the same. In line with the conclusions in [6], the case referring to the CD OFF shows a correlation which has been greatly reduced, which confirms that the CD was responsible of most of the microvibrations.

The analysis shown in Fig. 12 leads us to the conclusion that our Earth-view estimator is not only capable of accurately retrieving the IASI instrument noise, but it can also assess details of the off-diagonal terms of the covariance matrix.

We can also conclude that the difference between Earth view and blackbody estimates of the radiometric noise in the spectral domain 1210–1600 cm^{-1} (Figs. 8 and 9) is partly explained by the pseudo-noise induced by microvibrations. Due to the generally faster and stronger sample-to-sample variations in atmospheric spectra in comparison to blackbody spectra, this pseudo-noise is stronger for atmospheric spectra and has a stronger impact on the total noise budget where the instrument noise is weak (Fig. 8). As expected, this difference drops down in the CD OFF case (Fig. 9). However, Fig. 9 reveals a slight (positive) misfit in the spectral segment 1300 and 1500 cm^{-1}. This is the result of not using this spectral interval in the retrieval analysis (see Fig. 10). This effect is not likely due to residual atmospheric variability. In fact, our FOR by FOR sampling strategy largely eliminates this variability as far as the final estimate of $\hat{\mathbf{S}}_{\delta y}$ is concerned. This ineffectiveness is confirmed by the excellent agreement of the spectral residuals analysis with that provided by in-flight blackbody spectra when we look at spectral bands which were used for the retrieval analysis. The overestimation in the range of 1300 and 1500 cm^{-1} is likely an effect of spectroscopic inconsistency of the continuum absorption of H_2O within the band at 6.7 µm. Of this band, the right

Fig. 10. Example of the IASI spectrum showing the spectral segments used for the retrieval and the corresponding spectral analysis.

Fig. 12. IASI noise correlation matrix in the range of 1150–1250 cm⁻¹. (a) Derived from the IASI real observations of the Earth view on 22 July 2007 with the CD on. (b) Computed from a theoretical model which simulates the IASI ghost effect. (c) Derived from the IASI real observations of the Earth view on 25 November 2014 with the CD off. The apodization effect correlating that the noise in neighboring channels has been removed from the computations shown in the three figures.

branch is used for the retrieval (see Fig. 10), whereas the left branch is not.

5. CONCLUSIONS

As with any other kind of instrument, IASI and related radiances are affected by measurement or observation errors. Taking into account that retrieval schemes are designed to greatly filter out these errors, we have that O-C, i.e., the spectral residuals, depends on the instrument noise mostly because of O rather than C. This makes it possible to extract from O-C just the noise affecting measurements. Despite this apparent simplicity, this paper has shown that the quantitative analysis of the variance–covariance of O-C is complicated by the fact that O and C are correlated.

We have presented a rigorous mathematical approach which quantifies O-C correlation and fully assesses the statistical properties of the spectral residuals as a suitable means to design and implement an effective estimator of the instrument noise. Apart from mathematical complexity resulting from O-C correlation, the problem can become even more complicated because

spectroscopic noise and meteorological variability can introduce additional sources of randomness.

Meteorological variability can be almost entirely eliminated from the problem by a proper sampling strategy of the observations. In our case, a sampling strategy per IASI FOR has solved the problem. Spectroscopic noise and/or inconsistency of the forward model are much more subtle and can lead to an overestimation of the final instrument noise. Nevertheless, we have shown that for IASI, a *localized* spectral residuals analysis, that is an analysis which considers a suitable Earth view which is covered in a 1 min span, does work to limit extra variability because of forward model errors.

In fact, we have shown that FOR by FOR sampling and *localization* lead to an O-C approach which has the same sensitivity and quality as that provided by a direct in-flight blackbody-based analysis of the radiometric noise.

We have also shown that by using O-C analysis we could analyze the impact on the radiometric noise when changing the IASI corner cube compensation device from the CD ON to the CD OFF instrument mode. We have shown that the *ghost effect*, due to the microvibration of the beam splitter,

has been almost totally eliminated when disabling the compensation device, leading to an improvement of IASI spectral and radiometric performances.

The capability of our Earth-view methodology in providing an accurate assessment of the IASI noise, including the ghost effect, has been proved by remarkable experimental agreement with in-flight blackbody calibration. We conclude that the Earth-view-based estimator for the observational covariance matrix is reliable and largely independent of the operational observational covariance matrix imposed on the retrieval system. A fact that opens perspectives for its application to present and future satellite infrared instrumentation, e.g., MTG-IRS, with the aim of providing complementary and backup analysis to check noise performance and stability and support spectroscopic and forward modeling assessment studies. In fact, only in the case where the standard deviation of the spectral residuals closely fit the instrument noise can we interpret O-C mean differences (that is the spectral bias) as spectroscopic or forward model inconsistencies and not mere unresolved atmospheric variability.

APPENDIX A: DERIVATION OF EQ. (22)

With the help of the well-known matrix identity (e.g., [29])

$$(\mathbf{K}^t\tilde{\mathbf{S}}_\varepsilon^{-1}\mathbf{K} + \mathbf{S}_a^{-1})^{-1}\mathbf{K}^t\tilde{\mathbf{S}}_\varepsilon^{-1} = \mathbf{S}_a\mathbf{K}^t(\tilde{\mathbf{S}}_\varepsilon + \mathbf{K}\mathbf{S}_a\mathbf{K}^t)^{-1}, \quad \text{(A1)}$$

we can write

$$\mathbf{A}^{-1}\mathbf{B} = \mathbf{S}_a\mathbf{K}^t\mathbf{M}^{-1}, \quad \text{(A2)}$$

with

$$\mathbf{M} = (\tilde{\mathbf{S}}_\varepsilon + \mathbf{K}\mathbf{S}_a\mathbf{K}^t), \quad \text{(A3)}$$

and $\mathbf{A}$ and $\mathbf{B}$ defined by Eq. (11).

1. Case Where $\tilde{\mathbf{S}}_\varepsilon = \mathbf{S}_\varepsilon$

We consider this case first because it is a good introduction to the derivation of the most general case with $\tilde{\mathbf{S}}_\varepsilon \neq \mathbf{S}_\varepsilon$. Using the operator $\mathbf{M}$, Eq. (21) can be written as

$$\mathbf{S}_{\delta y} = (\mathbf{I} - \mathbf{K}\mathbf{S}_a\mathbf{K}^t\mathbf{M}^{-1})\mathbf{M}(\mathbf{I} - \mathbf{K}\mathbf{A}^{-1}\mathbf{B})^t, \quad \text{(A4)}$$

which by multiplying the two first terms and using the definition of $\mathbf{M}$ yields

$$\begin{aligned}\mathbf{S}_{\delta y} &= (\mathbf{M} - \mathbf{K}\mathbf{S}_a\mathbf{K}^t\mathbf{M}^{-1}\mathbf{M})(\mathbf{I} - \mathbf{K}\mathbf{A}^{-1}\mathbf{B})^t \\ &= (\mathbf{S}_\varepsilon + \mathbf{K}\mathbf{S}_a\mathbf{K}^t - \mathbf{K}\mathbf{S}_a\mathbf{K}^t)(\mathbf{I} - \mathbf{K}\mathbf{A}^{-1}\mathbf{B})^t \\ &= \mathbf{S}_\varepsilon(\mathbf{I} - \mathbf{K}\mathbf{A}^{-1}\mathbf{B})^t \\ &= \mathbf{S}_\varepsilon - \mathbf{S}_\varepsilon\mathbf{S}_\varepsilon^{-1}\mathbf{K}\mathbf{A}^{-1}\mathbf{K}^t \\ &= \mathbf{S}_\varepsilon - \mathbf{K}\mathbf{A}^{-1}\mathbf{K}^t, \end{aligned} \quad \text{(A5)}$$

where we have used $\mathbf{B} = \mathbf{K}^t\tilde{\mathbf{S}}_\varepsilon^{-1}$ and $\tilde{\mathbf{S}}_\varepsilon = \mathbf{S}_\varepsilon$.

To derive the alternate formula of Eq. (24), we again make use of $\mathbf{M}$ and rewrite Eq. (21) according to

$$\mathbf{S}_{\delta y} = (\mathbf{I} - \mathbf{K}\mathbf{S}_a\mathbf{K}^t\mathbf{M}^{-1})\mathbf{M}\mathbf{M}^{-1}\mathbf{M}(\mathbf{I} - \mathbf{M}^{-1}\mathbf{K}\mathbf{S}_a\mathbf{K}^t), \quad \text{(A6)}$$

which by multiplying out the first terms by the second and the fourth by the fifth, yields

$$\mathbf{S}_{\delta y} = (\mathbf{M} - \mathbf{K}\mathbf{S}_a\mathbf{K}^t)\mathbf{M}^{-1}(\mathbf{M} - \mathbf{K}\mathbf{S}_a\mathbf{K}^t), \quad \text{(A7)}$$

which by using the definition of $\mathbf{M}$ (note that we are using $\tilde{\mathbf{S}}_\varepsilon = \mathbf{S}_\varepsilon$) becomes

$$\mathbf{S}_{\delta y} = \mathbf{S}_\varepsilon\mathbf{M}^{-1}\mathbf{S}_\varepsilon = \mathbf{S}_\varepsilon(\mathbf{S}_\varepsilon + \mathbf{K}\mathbf{S}_a\mathbf{K}^t)^{-1}\mathbf{S}_\varepsilon. \quad \text{(A8)}$$

2. General Case Where $\tilde{\mathbf{S}}_\varepsilon \neq \mathbf{S}_\varepsilon$

The complication of the formalism arises from the fact that $\mathbf{A}$ and $\mathbf{B}$ contain $\tilde{\mathbf{S}}_\varepsilon$, because they are defined for the retrieval system, whereas the middle term of Eq. (21), which derives from mathematical manipulation of the radiance vector, has $\mathbf{S}_\varepsilon$ inside. However, by adding and subtracting $\tilde{\mathbf{S}}_\varepsilon$ to the middle term in Eq. (21), we have

$$\begin{aligned}\mathbf{S}_{\delta y} = (\mathbf{I} - \mathbf{K}\mathbf{A}^{-1}\mathbf{B})((\tilde{\mathbf{S}}_\varepsilon + \mathbf{K}\mathbf{S}_a\mathbf{K}^t) \\ + (\mathbf{S}_\varepsilon - \tilde{\mathbf{S}}_\varepsilon))(\mathbf{I} - \mathbf{K}\mathbf{A}^{-1}\mathbf{B})^t,\end{aligned} \quad \text{(A9)}$$

which can be split out in two additive terms

$$\begin{aligned}\mathbf{S}_{\delta y} &= \mathbf{T}_1 + \mathbf{T}_2, \\ \mathbf{T}_1 &= (\mathbf{I} - \mathbf{K}\mathbf{A}^{-1}\mathbf{B})(\tilde{\mathbf{S}}_\varepsilon + \mathbf{K}\mathbf{S}_a\mathbf{K}^t)(\mathbf{I} - \mathbf{K}\mathbf{A}^{-1}\mathbf{B})^t, \\ \mathbf{T}_2 &= (\mathbf{I} - \mathbf{K}\mathbf{A}^{-1}\mathbf{B})(\mathbf{S}_\varepsilon - \tilde{\mathbf{S}}_\varepsilon)(\mathbf{I} - \mathbf{K}\mathbf{A}^{-1}\mathbf{B})^t.\end{aligned} \quad \text{(A10)}$$

The form $\mathbf{T}_1$ is completely equivalent to Eq. (A4). We need only to take into account that $\mathbf{S}_\varepsilon$ has to be changed to $\tilde{\mathbf{S}}_\varepsilon$. Therefore, as before, we have

$$\mathbf{T}_1 = \tilde{\mathbf{S}}_\varepsilon - \mathbf{K}\mathbf{A}^{-1}\mathbf{K}^t. \quad \text{(A11)}$$

The form $\mathbf{T}_2$ can be reduced just by multiplying out to yield

$$\begin{aligned}\mathbf{T}_2 = (\mathbf{S}_\varepsilon - \tilde{\mathbf{S}}_\varepsilon) - (\mathbf{S}_\varepsilon - \tilde{\mathbf{S}}_\varepsilon)(\mathbf{K}\mathbf{A}^{-1}\mathbf{B})^t - \mathbf{K}\mathbf{A}^{-1}\mathbf{B}(\mathbf{S}_\varepsilon - \tilde{\mathbf{S}}_\varepsilon) \\ + \mathbf{K}\mathbf{A}^{-1}\mathbf{B}(\mathbf{S}_\varepsilon - \tilde{\mathbf{S}}_\varepsilon)(\mathbf{K}\mathbf{A}^{-1}\mathbf{B})^t.\end{aligned} \quad \text{(A12)}$$

Adding $\mathbf{T}_1$ to $\mathbf{T}_2$ and using the definition of $\mathbf{B}$, we have Eq. (22).

IASI has been developed and built under the responsibility of CNES. It is flown onboard the Metop satellites as part of the EUMETSAT Polar System. The IASI L1 data are received through the EUMETCast near real-time data distribution service. External calibration IASI L1 data and corresponding engineering data are provided by the IASI Technical Expertise Centre at CNES.

REFERENCES

1. C. D. Rodgers, *Inverse Methods for Atmopsheric Sounding: Theory and Practice* (World Scientific, 2000).
2. G. Masiello, C. Serio, and P. Antonelli, "Inversion for atmospheric thermodynamical parameters of IASI data in the principal components space," Q. J. R. Meteorol. Soc. **138**, 103–117 (2012).
3. N. Bormann, A. Collard, and P. Bauer, "Estimates of spatial and interchannel observation-error characteristics for current sounder radiances for numerical weather prediction. II: application to AIRS and IASI data," Q. J. R. Meteorol. Soc. **136**, 1051–1063 (2010).
4. L. M. Stewart, S. L. Dance, N. K. Nichols, J. R. Eyre, and J. Cameron, "Estimating interchannel observation-error correlations for IASI radiance data in the Met Office system," Q. J. R. Meteorol. Soc. **140**, 1236–1244 (2014).
5. F. Hilton, R. Armante, R. August, C. Barnet, A. Bouchard, C. Camy-Peyret, V. Capelle, L. Clarisse, C. Clerbaux, P. F. Coheur, A. Collard, C. Crevoisier, G. Dufour, D. Edwards, F. Faijan, N. Fourrié, A. Gambacorta, M. Goldberg, V. Guidard, D. Hurtmans, S. Illingworth, N. Jacquinet-Husson, T. Kerzenmacher, D. Klaes, L. Lavanant, G. Masiello, M. Matricardi, A. McNally, S. Newman, E. Pavelin, S. Payan, E. Péquignot, S. Peyridieu, T. Phulpin, J. Remedios,

P. Schlüssel, C. Serio, L. Strow, C. Stubenrauch, J. Taylor, D. Tobin, W. Wolf, and D. Zhou, "Hyperspectral Earth Observation from IASI: four years of accomplishments," Bull. Am. Meteorol. Soc. **93**, 347–370 (2012).

6. C. Maraldi, E. Jacquette, and D. Coppens, "IASI in-flight cube corner compensation device stop performance report," IASI Technical Expertise Center, Doc. IA-RP-2000-4190-CNE (CNES, 2015).

7. E. Jacquette and J. Chinaud, IASI Quarterly Performance Report from 2012/09/01 to 2012/11/30 by IASI TEC (Technical Expertise Center) for IASI PFM-R on METOP A (CNES, 2013).

8. A. Hollingsworth and P. Lönnberg, "The statistical structure of short-range forecast errors as determined from radiosonde data. Part I: the wind field," Tellus **38A**, 111–136 (1986).

9. G. Desroziers, L. Berre, B. Chapnik, and P. Poli, "Diagnosis of observation, background and analysis-error statistics in observation space," Q. J. R. Meteorol. Soc. **131**, 3385–3396 (2005).

10. N. Bormann and P. Bauer, "Estimates of spatial and interchannel observation-error characteristics for current sounder radiances for numerical weather prediction. I: Methods and application to ATOVS data," Q. J. R. Meteorol. Soc. **136**, 1036–1050, (2010).

11. L. Wang and C. Cao, "On-Orbit calibration assessment of AVHRR longwave channels on MetOp-A using IASI," IEEE Trans. Geosci. Remote Sens. **46**, 4005–4013 (2008).

12. S. M. Illingworth, J. J. Remedios, and R. J. Parker, "Intercomparison of integrated IASI and AATSR calibrated radiances at 11 and 12 μm," Atmos. Chem. Phys. **9**, 6677–6683 (2009).

13. A. M. Larar, W. L. Smith, D. K. Zhou, X. Liu, H. Revercomb, J. P. Taylor, S. M. Newman, and P. Schlüssel, "IASI spectral radiance validation inter-comparisons: case study assessment from the JAIVEx field campaign," Atmos. Chem. Phys. **10**, 411–430 (2010).

14. B. A. Wielicki, D. F. Young, M. G. Mlynczak, K. J. Thome, S. Leroy, J. Corliss, J. G. Anderson, C. O. Ao, R. Bantges, F. Best, K. Bowman, H. Brindley, J. J. Butler, W. Collins, J. A. Dykema, D. R. Doelling, D. R. Feldman, N. Fox, X. Huang, R. Holz, Y. Huang, Z. Jin, D. Jennings, D. G. Johnson, K. Jucks, S. Kato, D. B. Kirk-Davidoff, R. Knuteson, G. Kopp, D. P. Kratz, X. Liu, C. Lukashin, A. J. Mannucci, N. Phojanamongkolkij, P. Pilewskie, V. Ramaswamy, H. Revercomb, J. Rice, Y. Roberts, C. M. Roithmayr, F. Rose, S. Sandford, E. L. Shirley, W. L. Smith, Sr., B. Soden, P. W. Speth, W. Sun, P. C. Taylor, D. Tobin, and X. Xiong, "Achieving climate change absolute accuracy in orbit," Bull. Am. Meteorol. Soc. **94**, 1519–1539 (2013).

15. M. W. Shephard, S. A. Clough, V. H. Payne, W. L. Smith, S. Kireev, and K. E. Cady-Pereira, "Performance of the line-by-line radiative transfer model (LBLRTM) for temperature and species retrievals: IASI case studies from JAIVEx," Atmos. Chem. Phys. **9**, 7397–7417 (2009).

16. G. Masiello, C. Serio, A. Carissimo, G. Grieco, and M. Matricardi, "Application of φ-IASI to IASI: retrieval products evaluation and radiative transfer consistency," Atmos. Chem. Phys. **9**, 8771–8783 (2009).

17. A. Carissimo, I. De Feis, and C. Serio, "The physical retrieval methodology for IASI: the δ-IASI code," Environ. Modell. Softw. **20**, 1111–1126, (2005).

18. R. Rizzi, L. Palchetti, B. Carli, R. Bonsignori, J. E. Harries, J. Leotin, S. C. Peskett, C. Serio, and A. Sutera, "Feasibility of the spaceborne radiation explorer in the far infrared (REFIR)," Proc. SPIE **4485**, 202–209 (2002).

19. U. Amato, G. Masiello, C. Serio, and M. Viggiano, "The σ-IASI code for the calculation of infrared atmospheric radiance and its derivatives," Environ. Modell. Softw. **17**, 651–667 (2002).

20. V. Wulfmeyer, H. Bauer, P. Di Girolamo, and C. Serio, "Comparison of active and passive water vapor remote sensing from space: An analysis based on the simulated performance of IASI and space borne differential absorption lidar," Remote Sens. Environ. **95**, 211–230 (2005).

21. G. Grieco, G. Masiello, M. Matricardi, C. Serio, D. Summa, and V. Cuomo, "Demonstration and validation of the φ-IASI inversion scheme with NAST-I data," Q. J. R. Meteorol. Soc. **133**, 217–232 (2007).

22. G. Grieco, G. Masiello, and C. Serio, "Interferometric vs spectral IASI radiances: effective data-reduction approaches for the satellite sounding of atmospheric thermodynamical parameters," Remote Sens. **2**, 2323–2346 (2010).

23. G. Masiello, M. Matricardi, and C. Serio, "The use of IASI data to identify systematic errors in the ECMWF forecasts of temperature in the upper stratosphere," Atmos. Chem. Phys. **11**, 1009–1021 (2011).

24. G. Masiello, C. Serio, T. Deleporte, H. Herbin, P. Di Girolamo, C. Champollion, A. Behrendt, P. Bosser, O. Bock, V. Wulfmeyer, M. Pommier, and C. Flamant, "Validation of the IASI retrieved water vapor profiles using the COPS campaign data," Meteorologische Zeitschrift **22**, 471–487 (2013).

25. U. Amato, D. De Canditiis, and C. Serio, "Effect of apodization on the retrieval of geophysical parameters from Fourier-transform spectrometers," Appl. Opt. **37**, 6537–6543 (1998).

26. S. A. Clough, M. W. Shephard, E. J. Mlawer, J. S. Delamere, M. J. Iacono, K. Cady-Pereira, S. Boukabara, and P. D. Brown, "Atmospheric radiative transfer modeling: a summary of the AER codes, short communication," J. Quant. Spectrosc. Radiat. Transfer **91**, 233–244 (2005).

27. K. Masuda, T. Takashima, and Y. Takayma, "Emisivity of pure and sea waters for the model sea surface in the infrared window regions," Remote Sens. Environ. **24**, 313–329 (1988).

28. E. Dufour, A. Klonecki, B. Tournier, C. Standfuss, C. Serio, and G. Masiello, "Validation of MTG-IRS level 1 B data using Earth scenes," Final Report NOV-7316-NT-4711, Issue 1, Rev. 0, p. 136, EUMETSAT contract EUM/CO/13/4600001292/SAT (NOVELTIS, 2014).

29. A. Tarantola, *Inverse Problem Theory: Methods for Data Fitting and Model Parameter Estimation* (Elsevier, 1987).